RESEARCH ARTICLE | MARCH 19 2025

Refined radial basis function-generated finite difference analysis of non-Newtonian natural convection

Miha Rot ; Gregor Kosec

Physics of Fluids 37, 033130 (2025)
https://doi.org/10.1063/5.0257896

Physics of Fluids ARTICLE pubs.aip.org/aip/pof

Refined radial basis function-generated finite difference analysis of non-Newtonian natural convection

Cite as: Phys. Fluids **37**, 033130 (2025); doi: 10.1063/5.0257896
Submitted: 13 January 2025 · Accepted: 24 February 2025 ·
Published Online: 19 March 2025

Miha Rot[1,2,a)] and Gregor Kosec[2]

AFFILIATIONS

[1]Jozef Stefan International Postgraduate School, Jamova cesta 39, 1000 Ljubljana, Slovenia
[2]Jožef Stefan Institute, Parallel and Distributed Systems Laboratory, Jamova cesta 39, 1000 Ljubljana, Slovenia

[a)]Author to whom correspondence should be addressed: miha.rot@ijs.si

ABSTRACT

In this paper, we present a refined radial basis function-generated finite difference solution for a non-Newtonian fluid in a closed differentially heated cavity. The non-Newtonian behavior is modeled with the Ostwald–de Waele power law and the buoyancy with the Boussinesq approximation. The problem domain is discretized with scattered nodes without any requirement for a topological relation between them. This allows a trivial generalization of the solution procedure to complex irregular three dimensional (3D) domains, which is also demonstrated by solving the problem in a two dimensional (2D) and 3D geometry mimicking a porous filter. The results in 2D are compared with two reference solutions that use the finite volume method in a conjunction with two different stabilization techniques, where we achieved good agreement with the reference data. The refinement is implemented on top of a dedicated meshless node positioning algorithm using piecewise linear node density function that ensures sufficient node density in the center of the domain while maximizing the node density in a boundary layer where the most intense dynamic is expected. The results show that with a refined approach, more than five times fewer nodes are required to obtain the results with the same accuracy compared to the regular discretization. The paper also discusses the convergence with refined discretization for different scenarios for up to 2×10^5 nodes, the impact of method parameters, the behavior of the flow in the boundary layer, the behavior of the viscosity, and the geometric flexibility of the proposed solution procedure.

I. INTRODUCTION

Natural convection, a type of flow driven by the temperature-dependent density of a fluid, is a cornerstone of many natural and industrial processes. The most vivid examples in nature where it plays a crucial role are probably weather systems, e.g., sea and land breezes. In industry, it is of paramount importance in metal casting, various heating systems, food processing, etc.[1] The minimal model describing natural convection involves coupled heat transfer and fluid dynamics,[2] where simple fluids such as air and water are usually modeled as Newtonian fluids, i.e., the viscosity of the fluid is constant. However, such an approximation becomes insufficient when dealing with more complex fluids[3] like melts of large and complicated molecules, polymers,[4] suspensions, foams, biological fluids such as blood,[5] food,[6,7] etc. In such fluids, also called non-Newtonian fluids, the relationship between stress and strain is no longer linear, and the viscous stress becomes related to the shear rate.[8] The behavior of purely viscous non-Newtonian fluids can generally be divided into two groups based on how their viscosity changes with increasing shear rate, namely, shear-thinning, where viscosity decreases, and shear-thickening, where viscosity increases.

Because of its importance in industry and in understanding nature, the study of non-Newtonian natural convection (NNC) has attracted much research attention. Since closed-form solutions are rare and limited to extreme simplifications, the problem is usually treated numerically.[9] The dynamics of non-Newtonian fluids have been studied in various fields, from non-Newtonian blood flow in arteries[10] to injection molding of plastics.[4] In particular, natural convection in cavities has been thoroughly analyzed due to its direct application in industry.[9]

From the numerical analysis point of view, the most commonly reported approaches to solving NNC in cavities are based on the finite volume method (FVM) for the discretization of the relevant partial

differential operators and semi-implicit method for pressure-linked equations (SIMPLE) for pressure–velocity coupling.[11] A comprehensive study of NNC solved with FVM and quadratic upstream interpolation for convective kinematics (QUICK) to treat the convective terms was presented in Ref. 12, and with upwind stabilization of convective terms in Ref. 13. The FVM with QUICK was further investigated in Ref. 14 in solving NNC with internal rotating heater and cooler. Moraga *et al.*[15] demonstrated the multigrid FVM with a fifth power differentiation scheme for convective transport in the solution of NNC with phase change. A similar numerical approach was also used in the solution of NNC in three dimensions (3D).[16] In conjunction with the finite difference method (FDM) and upwind stabilization, the solution of NNC with internal heat source was recently demonstrated in Ref. 17. The NNC was also solved with a finite element method (FEM)[18,19] as well as with the lattice Boltzmann method (LBM).[20]

All the aforementioned solution methods are mesh-based, i.e., the nodes are structured into polygons that completely cover the computational domain, a process also known as meshing. In FDM, FVM, and LBM, a regular grid is often used, making meshing a trivial task, but at the cost of complications with irregular geometries and potential refinement. At FEM, meshing is mandatory and often also the most time-consuming part of the entire solution process, especially for realistic 3D geometries, which generally cannot be automatically meshed and therefore often require the user's help. An alternative to the mesh-based methods is the meshless approach.[21] The conceptual difference between mesh-based and meshless methods is that in the latter all relationships between nodes are defined solely by inter-nodal distances. An important implication of this distinction is that the meshless methods can work with scattered nodes, which greatly facilitates the consideration of complex 3D geometries and adaptivity.

In this paper, we introduce a novel refined radial basis function-generated finite difference (RBF-FD)[22] meshless solution of NNC in two dimensional (2D) and 3D irregular domains computed on automatically generated scattered nodes,[23] using the artificial compressibility method (ACM) for pressure–velocity coupling,[24–26] and explicit time stepping. No stabilization of the convective terms is used to minimize the impact of numerical diffusion in the results. We present a unified NNC solution procedure for 2D and 3D that can be easily extended to arbitrary geometries and inherently supports *hp*-adaptivity.[27,28]

Results for a reference 2D case are compared with data from Turan *et al.*[13] and Kim *et al.*,[12] showing that our results are in the range of the comparative data. Therefore, in addition to a novel solution procedure, we also extend the range of available numerical solutions for the given problem with a completely different numerical approach. Note that the reference solutions differ only in the stabilization of the convective terms (Upwind vs QUICK); otherwise, in both papers, results are computed with FVM and SIMPLE coupling.

In Sec. II, a mathematical model of NNC is discussed, followed by a presentation of the meshless numerical method and solution procedure in Sec. III. The analysis of results for the reference 2D case and a showcase of the method's versatility on more complex cases are shown in Secs. IV and V.

II. PROBLEM FORMULATION

The dynamics of natural convection in non-Newtonian fluids are governed by a system of three partial differential equations describing the continuity of mass, the conservation of momentum, and the conservation of energy,

$$\nabla \cdot \boldsymbol{v} = 0, \tag{1}$$

$$\rho\left(\frac{\partial \boldsymbol{v}}{\partial t} + \boldsymbol{v}\cdot\nabla\boldsymbol{v}\right) = -\nabla p + \nabla\cdot\left(\eta\left(\nabla\boldsymbol{v} + (\nabla\boldsymbol{v})^T\right)\right) - \boldsymbol{g}\rho\beta T_\Delta, \tag{2}$$

$$\rho c_p\left(\frac{\partial T}{\partial t} + \boldsymbol{v}\cdot\nabla T\right) = \nabla\cdot(\lambda\nabla T), \tag{3}$$

$$\eta = \eta_0\left(\frac{1}{2}||\nabla\boldsymbol{v} + (\nabla\boldsymbol{v})^T||\right)^{\frac{n-1}{2}}, \tag{4}$$

with $\boldsymbol{v}$, T, p, η, ρ, $\boldsymbol{g}$, β, T_Δ, c_p, η_0, and n, representing the flow velocity field, temperature field, pressure field, viscosity field, density, gravity, thermal expansion coefficient, temperature offset, heat capacity, viscosity constant, and non-Newtonian exponent, respectively.

The buoyancy force that drives the natural convection dynamics is relatively weak and ensures that the maximum velocity remains well below the speed of sound. This allows us to model the fluid as incompressible[29] and reduce the continuity equation to (1). The fluid motion is described by the Navier–Stokes equation (2), which is modified from its usual form by the addition of a force term describing the buoyancy caused by the thermal expansion. This force is approximated by the Boussinesq approximation,[30] which is based on the assumption that the acceleration of a fluid driven by natural convection remains insignificant compared to gravity and consequently the small thermal fluctuations of the density only play a role when amplified by the strong gravity in the buoyancy term. The Boussinesq approximation couples the fluid motion described by the Navier–Stokes equation (2) with the temperature described by the energy equation (3) and thus establishes the model for natural convection driven by the presence of a temperature gradient.

The constant viscosity η is replaced by the Ostwald–de Waele power law model[9] defined in Eq. (4). The shear dependence is captured by the exponentiated tensor norm of the shear rate tensor[31] and controlled by the exponent n, which controls the extent of the non-Newtonian behavior, and η_0, which is used as a scaling factor.

The model reduces to a Newtonian fluid when $n = 1$ and can be used to describe both shear-thickening behavior with $n > 1$ and shear-thinning behavior with $n < 1$. We focus on the latter as it leads to stronger convection, i.e., more interesting flow behavior, and is more common in realistic fluids. A visualization of the viscosity dependence for an arbitrarily chosen range of shear rate norms can be found on the right-hand panel of Fig. 1 for a range of exponents that we will use in further analysis. It can be seen from the figure that while n has a dramatic impact on the effective viscosity, there is also a problem with the divergent viscosity at low shear rates in the shear-thinning regime. This is mainly a problem for the initial, transient part of the simulation, where a flow pattern emerges from the initially stationary fluid and can be solved by downward bounding[32] the shear rate norm used in the power law to 10^{-10}.

Model parameters that reflect the behavior of a realistic fluid are typically determined by fitting the model to experimental data. Ostwald–de Waele power law model is the most basic approach to characterizing shear-dependent behavior, and it is only appropriate for the intermediate shear rate regime. To accurately capture the asymptotic behavior of realistic shear-thinning fluids at both low and high

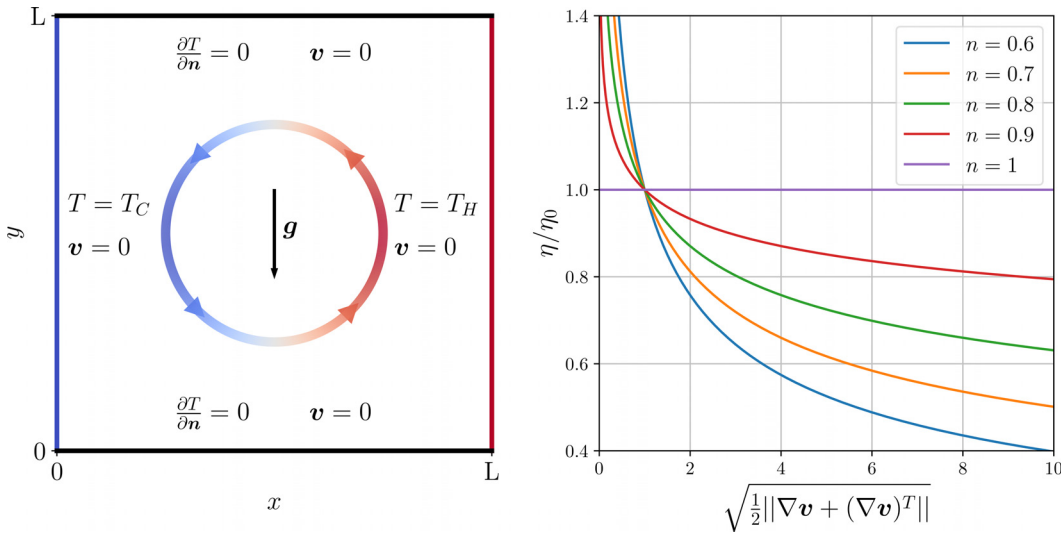

FIG. 1. *Left:* A schematic representation of the De Vahl Davis differentially heated cavity case with velocity and temperature boundary conditions. *Right:* Relationship between viscosity and shear rate for a $n = 1$ Newtonian and a selection of shear-thinning $n < 1$ non-Newtonian cases.

shear rates, the specialized models with more intricate algebraic structure due to additional parameters are used.[3] Nevertheless, from a numerical standpoint, these more complex models do not significantly affect the solution methodology nor do they introduce any additional numerical challenges.

The natural convection described with the system of equations described above is applied to the De Vahl Davis case,[33] a differentially heated square cavity with height and width $L = 1$, shown schematically in the left graph of Fig. 1. The left wall is kept at a constant temperature $T_C = -1$, while the right wall is kept at a higher constant temperature $T_H = 1$, inducing the heat transfer that drives the dynamics of the system. The top and bottom boundaries are insulated. No-slip boundary conditions for velocity are imposed on all walls.

The difference in boundary temperatures creates a temperature gradient within the cavity that leads to natural convection. The convective flow appears due to the temperature-dependent changes in fluid density and the resulting buoyancy forces, which are described by the Boussinesq approximation term in Eq. (2). The fluid cools and becomes denser at the left wall, so it falls and moves to the right, where it is heated by the hot wall, rises, and completes the circular flow.

The circular flow caused by natural convection significantly increases the heat transfer between the differentially heated walls compared to conduction alone. The ratio between the two is known as the Nusselt number and provides a convenient reduction that expresses the convective heat transfer in a single scalar value. Such reduction can be further analyzed to determine the temporal behavior, as shown in Fig. 5, from which we can deduce when the steady state was reached. The Nusselt number used in the following analysis is calculated as the average of the values in the cold wall nodes,

$$\mathrm{Nu} = \frac{L}{T_H - T_C} \left| \frac{\partial T}{\partial x} \right|_{x=0}. \tag{5}$$

The problem is further characterized by two dimensionless numbers. The Prandtl number (Pr) is a material property that expresses the ratio between the heat and momentum transport properties of the fluid. The Rayleigh number (Ra) can be interpreted as the ratio of buoyancy and thermal diffusivity and is the product of the Grashof and Prandtl numbers. For the purposes of this study, it can be interpreted as an analogue of the Reynolds number for natural convection, with larger values implying wilder dynamics. Both Ra and Pr are a function of viscosity and must be modified to account for non-Newtonian viscosity,

$$\mathrm{Pr} = \frac{\eta_0}{\rho} \alpha^{n-2} L^{2-2n}, \tag{6}$$

$$\mathrm{Ra} = \frac{\rho g \beta \Delta T L^{2n+1}}{\alpha^n \eta_0}, \tag{7}$$

with $\alpha = \frac{\lambda}{c_p \rho}$ as the thermal diffusivity. The definitions for the dimensionless numbers match the reference solution[13] to facilitate comparison, as does the dimensionless time,

$$\hat{t} = \frac{\alpha}{L^2} t, \tag{8}$$

and velocity,

$$\hat{v} = \frac{L c_p \rho}{\lambda} v. \tag{9}$$

We omit the Caret notation, since dimensionless values are used wherever velocity or time are referred to in the following discussion.

III. NUMERICAL SOLUTION PROCEDURE

Our goal is to solve the problem (1)–(3) using an approach that is as general as possible, including the generality of the number of dimensions, the order of the method, and the shape of the considered domain, while supporting a spatially variable discretization. To achieve this, we employ the RBF-FD method with augmenting monomials, which is a meshless numerical method operating on scattered nodes.

The first step is to discretise the domain, which in the meshless context means populating with scattered nodes. Although in the early stages of meshless development some authors used even randomly generated nodes,[21] it is now generally accepted that despite the apparent robustness of meshless methods regarding the node positioning, nodes still need to be generated according to certain rules,[23] i.e., nodes have to "uniformly" cover the domain with minimal empty spaces and satisfy the minimum distance requirement to avoid ill-conditioning of the approximation. There are several specially designed algorithms for meshless discretization, ranging from expensive iterative[34] to advancing front[35] approaches. In this paper, we use a Poisson disk sampling based advancing font approach.[23,36–38] The core of the algorithm is the iteration, where candidate nodes are sampled around the already positioned nodes and only those that do not violate the minimal distance requirement are added to the list of discretization nodes. This conceptually simple approach has several convenient features. It is dimensionally agnostic, meaning that the formulation of the algorithm is the same regardless of the number of dimensions of the domain. It supports variable density node distributions, which are a cornerstone of the refined solutions discussed in Sec. IV C. It guarantees minimal spacing and is proven to be computationally efficient.

We begin the analyses with a constant density node distribution, shown in the left panel of Fig. 2, which, as we will see in Sec. IV C, is a sub-optimal strategy for the problem at hand with intense dynamics in the boundary layer (see Sec. IV A). An improved node placement strategy, shown in the central panel of Fig. 2 and discussed in Sec. IV C, uses prior knowledge of the system to devise a target node density that significantly reduces computational cost without sacrificing accuracy. This solution is still not ideal, as it requires physical intuition and manual input, but it demonstrates the potential for the eventual goal, which is an h-adaptive solution with an appropriate error indicator. In a rightmost plot of Fig. 2, we demonstrate discretization of an irregular domain that will be used in Sec. V.

Once the computational nodes are generated, we identify the approximation stencil, i.e., the nodes used in local approximation of differential operators. Here, we will resort to simplest stencil strategy, where for each node i, s neighboring nodes are identified as a stencil S_i. In addition to basic closest-node stencils, recent studies[39] suggest that advanced symmetric stencils might significantly enhance the stability of meshless approximations. However, most research still employs nearest neighbors stencils; thus, we will also use it in this paper.

In the next step, we construct a generalized finite difference approximation to numerically evaluate the linear differential operator $\mathcal{L}$ in the central node from the approximated function's values in stencil nodes,

$$(\mathcal{L}u)_i \approx \sum_{j=1}^{s} w_{i,j} u_{S_i(j)}, \tag{10}$$

where u_k denotes the value of the arbitrary approximated function u at the position of the kth node $\boldsymbol{p}_k$. The weights w are determined through the demand that Eq. (10) is exact for a set of basis functions, in our case radial basis functions (RBF),

$$\phi(j,k) = \phi\left(\frac{||\boldsymbol{p}_k - \boldsymbol{p}_j||}{\delta_j}\right), \tag{11}$$

where we introduced δ_j as a local scaling factor that decouples the approximation from the choice of coordinate system. It is set to an arbitrary local measure of distance, e.g., the distance to the closest stencil node, and is of the utmost importance when using RBFs that use a scaling parameter. Finally, we get a local linear system $\boldsymbol{A}\boldsymbol{w}_i = \boldsymbol{b}$,

$$\begin{bmatrix} \phi(S_i(1),S_i(1)) & \cdots & \phi(S_i(1),S_i(s)) \\ \vdots & \ddots & \vdots \\ \phi(S_i(s),S_i(1)) & \cdots & \phi(S_i(s),S_i(s)) \end{bmatrix} \begin{bmatrix} w_{i,1} \\ \vdots \\ w_{i,s} \end{bmatrix} = \begin{bmatrix} (\mathcal{L}\phi)(i,S_i(1)) \\ \vdots \\ (\mathcal{L}\phi)(i,S_i(s)) \end{bmatrix}, \tag{12}$$

for each node with the solution yielding stencil weights $\boldsymbol{w}_i$. The right-hand side vector $\boldsymbol{b}$ is formed by applying the linear operator $\mathcal{L}$ to the basis function and evaluating the result with an argument analogous to Eq. (11). We use polyharmonic splines (PHS) basis,

$$\phi(r) = r^k, \tag{13}$$

with odd order k, additionally augmented with polynomials for ensuring the polynomial reproduction and positive definiteness.[40] This setup is widely recognized as an RBF-FD method in meshless community.

The system for stencil weights is expanded with $N_p = \binom{m+d}{m}$ monomials[41] q, where m denotes the monomial order and d the spatial dimension. The monomials are scaled with a similar argumentation as RBFs in Eq. (11),

$$q_l(j,k) = q_l\left(\frac{\boldsymbol{p}_k - \boldsymbol{p}_j}{\delta_j}\right). \tag{14}$$

The $\boldsymbol{A}\boldsymbol{w}_i = \boldsymbol{b}$ system for approximation weights from Eq. (12) is augmented with monomials,

$$\begin{bmatrix} \boldsymbol{A} & \boldsymbol{Q} \\ \boldsymbol{Q}^T & 0 \end{bmatrix} \begin{bmatrix} \boldsymbol{w}_i \\ \boldsymbol{\lambda} \end{bmatrix} = \begin{bmatrix} \boldsymbol{b} \\ \boldsymbol{c} \end{bmatrix},$$
$$\boldsymbol{Q} = \begin{bmatrix} q_1(S_i(1),S_i(1)) & \cdots & q_{N_p}(S_i(1),S_i(1)) \\ \vdots & \ddots & \vdots \\ q_1(S_i(s),S_i(1)) & \cdots & q_{N_p}(S_i(s),S_i(1)) \end{bmatrix}, \tag{15}$$
$$\boldsymbol{c} = \begin{bmatrix} (\mathcal{L}q_1)(S_i(1),S_i(1)) \\ \vdots \\ (\mathcal{L}q_{N_p})(S_i(1),S_i(1)) \end{bmatrix},$$

with the additional weights $\boldsymbol{\lambda}$ treated as Lagrange multipliers and discarded after computation.

Augmentation with an order of at least $m = \frac{k-1}{2}$ is required to guarantee the positive definiteness for a PHS with order k. Higher orders of augmentation m provide better convergence characteristics,[42,43] with the order of convergence

$$\mathcal{O}(h^{m+1-\ell}), \tag{16}$$

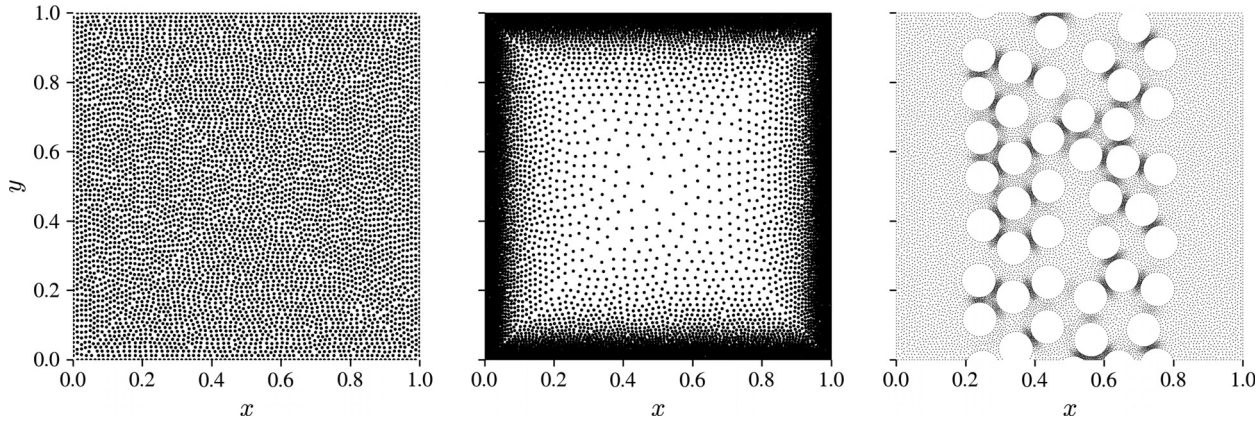

FIG. 2. A comparison between node distributions in domains populated with a constant node density on the left, refined density in the middle, and the obstructed domain with refined narrow channels on the right.

for $m \geq l$, where ℓ is the order of the linear operator $\mathcal{L}$. The higher accuracy comes at the cost of increased computational complexity, since the required stencil size is $s >= N_p$, with $s > 2N_p$ as the often recommended value.[44] Increased stencil size affects both the pre-computation of the approximation weights, with complexity $\mathcal{O}((s+N_p)^3)$, and the eventual scalar product $\mathcal{O}(s)$ evaluation. We will use $k = 3$, which is the minimum odd value that can be used to approximate second order derivatives, for all numerical results presented in this paper and compare the results for monomial orders $m = 2$ and $m = 4$. The support size is chosen conservatively as $s = 2N_p + 1$ unless otherwise specified. Nevertheless, augmenting monomials open an opportunity for *hp*-adaptivity, since their order directly controls the order of the method.[45]

Now that we have the RBF-FD approximation for derivatives, next step is to formulate a solution procedure for the problem at hand. The pressure–velocity coupling in the incompressible Navier–Stokes system is performed using the artificial compressibility method (ACM)[24–26] that was first introduced by Chorin[46] but is now experiencing resurgence due to its explicit and local nature that allows for easy parallelization and general-purpose graphics processing unit (GPGPU) usage.[47,48] The method works by artificially introducing a slight compressibility into the otherwise incompressible system in order to calculate the pressure field.

Since the focus of this study lies in the spatial discretization, we use the simple first-order explicit Euler method for the temporal discretization of the Navier–Stokes equation. The intermediate velocity

$$\boldsymbol{v}' = \boldsymbol{v} + \Delta t\left(\boldsymbol{\nabla}\cdot\left(\eta\left(\boldsymbol{\nabla v} + (\boldsymbol{\nabla v})^T\right)\right) - \boldsymbol{v}\cdot\nabla\boldsymbol{v} - \boldsymbol{g}\rho\beta T_\Delta\right), \quad (17)$$

is calculated by using the viscosity field η calculated from the previous step velocity according to Eq. (4), and the offset T_Δ in Boussinesq term based on the previous step temperature field. Note that the pressure term is omitted at this step. The time step

$$\Delta t = \min\left(\min_i\left(c_1\frac{h_i}{||\boldsymbol{v_i}||_2}\right), \min_i\left(c_2\frac{\rho h_i^2}{2\eta_i}\right)\right), \quad (18)$$

is calculated dynamically during each step of the iteration to adapt to the changing velocity and viscosity in computational nodes with a wide range of inter-nodal distances h_i. The time step constants are chosen as $c_1 = 0.05$ and $c_2 = 0.15$ based on trial and error. Values of the dynamic time step during the simulation with a constant discretization density using $h = 0.005$ are shown on the right graphs of Fig. 5. The variable time step is beneficial for most of the displayed cases as the most stringent requirements only occur during the relatively short period of initial flow formation. Note that the h^2 term in the viscous limit is likely to dominate the time step selection for very dense discretizations and might prove to be a limiting factor.

We omitted the pressure term from the initial intermediate velocity $\boldsymbol{v}'$ because the subsequent pressure–velocity coupling is done iteratively. First, the intermediate velocity is corrected with the previous pressure field,

$$\boldsymbol{v} = \boldsymbol{v}' - \frac{\Delta t}{\rho}\nabla p, \quad (19)$$

then the pressure field is corrected to counteract any divergence present in the velocity,

$$p \leftarrow p - \Delta t C^2 \rho(\nabla\cdot\boldsymbol{v}), \quad (20)$$

while enforcing

$$\frac{\partial p}{\partial \hat{\boldsymbol{n}}} = 0, \quad (21)$$

on the boundary, with $\hat{\boldsymbol{n}}$ being the corresponding surface normal vector. The strength of the artificial compressibility effects is recomputed at every step and governed with the artificial speed of sound C,[49]

$$C = \gamma\max(\max_i(||\boldsymbol{v_i}||_2), ||\boldsymbol{v}_{ref}||_2), \quad (22)$$

where γ is the compressibility parameter, and $\boldsymbol{v}_{ref}$ is a reference velocity introduced to prevent potential issues caused by C reaching zero. We use $\gamma = 5$ for all computations presented in this paper. If a time-accurate solution was required, the pressure–velocity coupling iteration would have to be repeated until the maximum divergence of the velocity field dropped below a desired level. In steady state cases like the

DVD in examined regime, a single iteration is sufficient as we are not really interested in the transient regime.

The new velocity is then used in the advection part of the energy transfer equation, again discretized with the explicit Euler method, which is then used to calculate the new temperature field. The same dynamic time step Δt calculated for the momentum equation can also be used for the energy equation as the latter is well within stability limits of the former when dealing with $\mathrm{Pr} = 100 \gg 1$ case.

IV. RESULTS

A. General flow behavior

We will study the impact of non-Newtonian behavior on three flow cases specified with Rayleigh and Prandtl dimensionless numbers as defined in Sec. II. Rayleigh numbers $\mathrm{Ra} = \{10^4, 10^5, 10^6\}$ are chosen to capture changes in the upper range of steady natural convection regime, while $\mathrm{Pr} = 100$ remains constant and is chosen to facilitate comparison with the existing reference solution.[13] The non-Newtonian behavior is examined with five values for the non-Newtonian exponent $n = \{0.6, 0.7, 0.8, 0.9, 1\}$ progressing from the $n = 0.6$ case that exhibits the strongest shear-thinning behavior to the Newtonian $n = 1$ case. Note that the most extreme case with $\mathrm{Ra} = 10^6$ and $n = 0.6$ is close to the edge of the steady regime. Further increases in Ra or decreases in n would result in an oscillatory flow.[12]

A sample of the resulting flow profiles can be seen in Fig. 3 where the velocity magnitude is displayed as a heat-map and overlaid with temperature contours. All cases exhibit the previously described circulation caused by natural convection, but there are drastic differences in the maximum velocity and the thickness of boundary layers as Ra and shear-thinning increase.

Both effects are expected and can be explained by the definition of varied parameters. The Rayleigh dimensionless number is defined as the product of Prandtl, which we keep constant, and Grashof dimensionless numbers. The latter expresses a ratio between buoyant and viscous forces and explains why increased Ra results in cases where fluid in the boundary layer convects away before conducting much heat to the neighboring fluid. Similarly, reduced n decreases viscous penalty for high velocity gradients close to the constant temperature edges, leading to a further reduction in boundary layer thickness.

Velocity fields also offer the first opportunity to verify the results. We compare the vertical velocity cross section at $y = 0.5$ with the reference solution[13] in Fig. 4. The position and value of the largest vertical velocity in the reference solution are added with an estimated error caused by the process of extracting the data from a similar cross section plot. Our results match the reference solution across the whole range of the considered parameters with the exception of the $\mathrm{Ra} = 10^6$ and $n = 0.6$ case with problematic convergence that is discussed and solved in the following sections.

In the subsequent analysis, we utilize the Nusselt number as a scalar observable to simplify the description of the system's behavior, facilitating temporal observation and comparison between different cases. One such example is shown in Fig. 5 where we track the evolution of the Nusselt number to determine when we reach a steady state. We can also observe the effects of stronger shear-thinning. Cases with lower n are faster to reach the stationary state as it is easier for convection to start, with the lower effective viscosity, and to play a bigger part in heat transfer as reflected in higher Nusselt values. The initial Nusselt number is high due to the high temperature gradient at the constant temperature boundary when starting from a zero-temperature zero-velocity initial condition. The value then decreases as the importance of conductive heat transport increases until circulation is established. Alternatively, we could start with the diffusive field as the initial condition for temperature, but this would only lead to a more violent flow formation with little benefit to accelerating the convergence to the convection dominated steady state.

B. Convergence under *h* refinement

The node density convergence analysis is performed to analyze node independence. We repeatedly run the same cases with decreasing inter-nodal distance h and examine how the average Nusselt number on the cold boundary changes with increasing number of computational nodes. The velocity and temperature fields are initially set to zero and the simulation is ran to $t = 0.1$ which is determined to be sufficient to ensure that a stationary state has been reached as seen in Fig. 5.

The convergence behavior for Newtonian ($n = 1$) cases shown in the bottom row of Fig. 6 is very tame, as the coarsest considered discretization already provides results with less than 10% discrepancy compared to the finest. Unfortunately, this is no longer the case as we progress toward non-Newtonian cases with a thinner boundary layer. The variation of the observed values increases, and the convergence rate decreases. This culminates in the most extreme case with $\mathrm{Ra} = 10^6$ and $n = 0.6$, shown in the upper right graph of Fig. 6, where adequate convergence is not achieved with the considered node counts. This can be further corroborated with the reference mismatch already observed for this case in Fig. 4. Proceeding to even higher node densities, requiring longer computational times, is wasteful, especially as the utilized numerical method allows for an elegant optimization described in following sections.

In next step, we compare different monomial augmentation orders $m = 2$ and $m = 4$, shown as different colors in Fig. 6. We consider the finest available discretization to produce an "accurate" solution and study the rate of convergence relative to that in the left graph of Fig. 7. From the log–log plot of the average Nusselt number offset against the inter-nodal distance h, we can determine that even though the higher augmentation order leads to a smaller initial error, the rate of convergence is similar for both. The discrepancy from the expected order, expressed with Eq. (16), is most likely caused by non-linearities in the system.

There is an interesting transition in convergence curves shown in Fig. 6 as we move toward the upper right corner, corresponding with cases that exhibit a thinner boundary layer with higher velocities. The calculated Nusselt numbers initially rise as we increase node density before falling toward the value they eventually converge to. This behavior can be better understood by examining the velocity cross section convergence, shown in the middle and right graphs of Fig. 7, for two of the $n = 0.6$ cases where it is most apparent. The velocity profiles show that the boundary layer initially becomes narrower and faster until a sufficient number of nodes is present to adequately capture the dynamics. This behavior provides us with additional motivation for refining the discretization close to the heated and cooled boundaries. Furthermore, the hypothesized issues with derivative approximation appear to also have a connection with the stencil size and/or approximation order as the Nusselt number peaks visible in Fig. 6 move

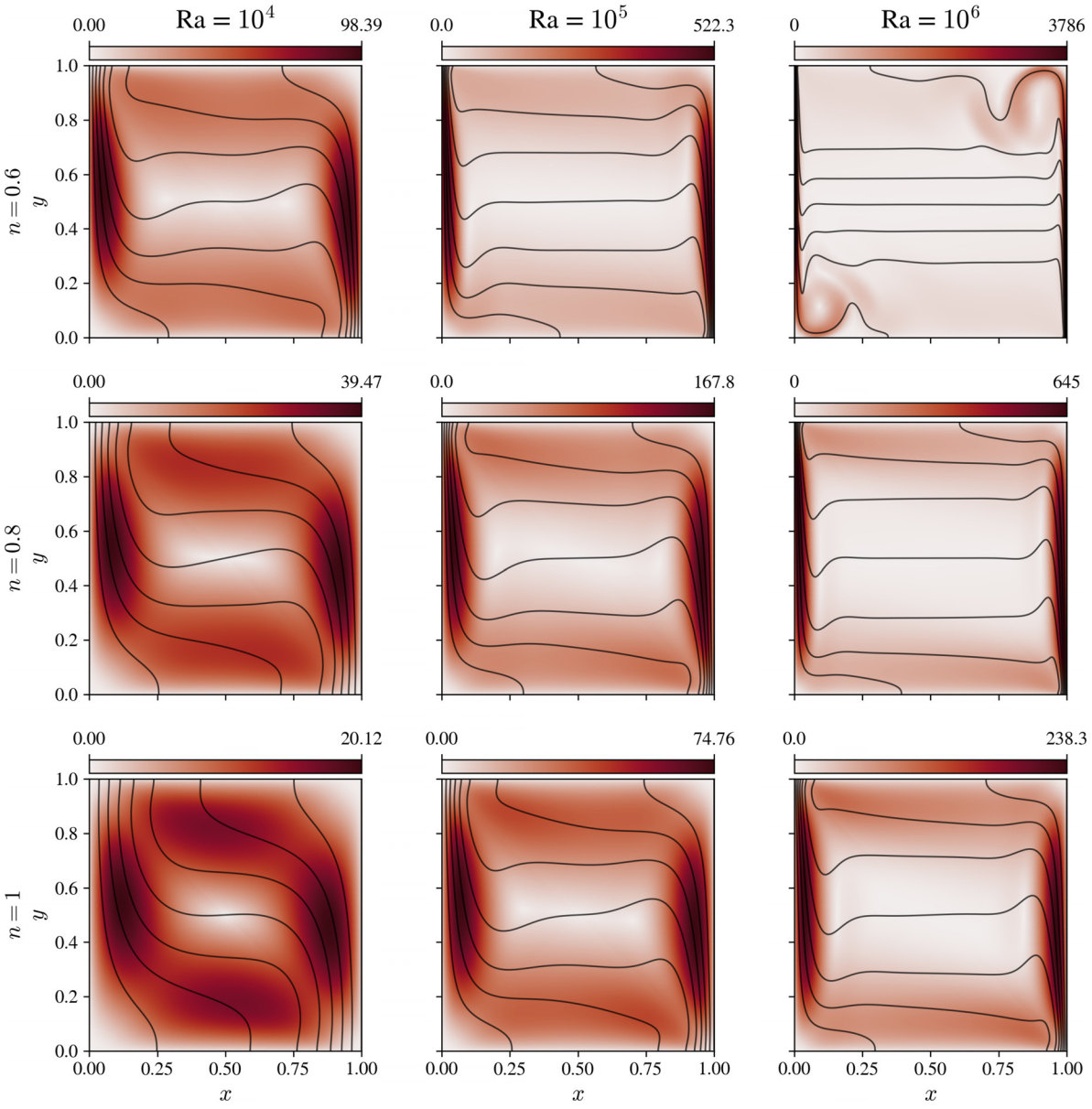

FIG. 3. Flow profiles for a selection of cases. Velocity magnitude is visualized with a heat-map, while the overlaid contours display the changes in temperature. Each sub-figure has a distinct velocity range specified by the colorbar above.

toward higher densities when augmented with a higher monomial order.

Furthermore, we examine the violation of symmetry,

$$u(x, y) = -u(1 - x, 1 - y), \tag{23}$$

as an alternative method for assessing the fitness of the solution. This is additionally motivated by the fact that the $\mathrm{Ra} = 10^6$ and $n = 0.6$ case with problematic convergence exhibits clearly visible asymmetry in velocity and temperature profiles shown in Fig. 3. First, we introduce a measure of symmetry violation by interpolating the vertical velocity v_y at an arbitrarily chosen y and $1 - y$ and calculating the relative error as

$$\epsilon = \frac{\max_{x\in[0,1]}(|v_y(x, y) + v_y(1 - x, 1 - y)|)}{\max_{x\in[0,1]}(|v_y(x, y)|)}, \tag{24}$$

where we normalize the maximum offset between a vertical velocity and its symmetric value with the maximum vertical velocity for a given case and selected y. This choice of denominator is preferable as it focuses on the symmetry errors in the relevant high velocity part of the domain while remaining relative for comparison between different

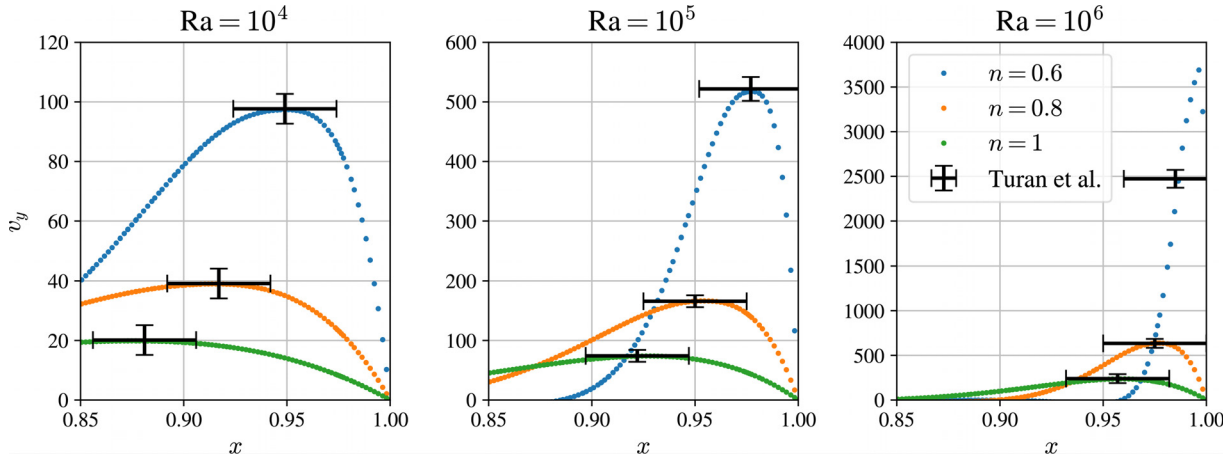

FIG. 4. Cross-section of vertical velocity v_y close to the right wall at $y = 0.5$ for a range of different Ra and n, calculated with Pr = 100 and $m = 4$. The error bars show the locations and values of maximum vertical velocity in corresponding plots from a reference solution.[13]

cases. The resulting symmetry errors as a function of the number of nodes are shown in Fig. 8 and corroborate the previous discussion that was based on convergences in Fig. 6. Additionally, we can also confirm the observation from the left graph of Fig. 7 as both $m = 2$ and $m = 4$ exhibit similar convergence behavior. Note that in addition to confirming the convergent behavior of the method, the introduced symmetry violation can also be interpreted as a lower bound for the error.

C. Refinement

Small flow structures and large velocity gradients (boundary layer) only occur in a relatively small part of the domain as seen in the right graph of Fig. 7 whose x-axis only covers about 10% of the domain's width. Needlessly covering the entire domain with the high node density, that is only required close to the cold and hot boundary, drastically increases the number of operations required at every time step without improving the results.

We introduce a variable node density expressed as the inter-nodal distance. In general, the inter-nodal distance would be a function of position but we use a symmetric configuration, shown schematically in the left graph of Fig. 9, that only depends on the distance to the closest boundary d. The idea is to position nodes with inter-nodal distance h_1 in a band within w of the boundary to ensure a sufficient

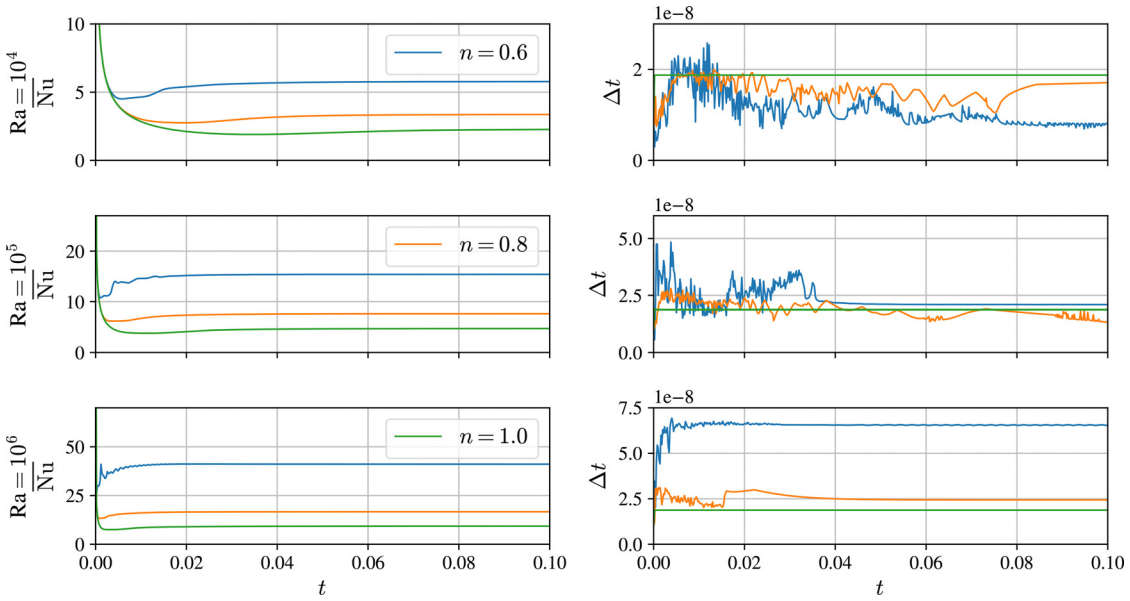

FIG. 5. *Left:* Time evolution of the average Nusselt number on the cold wall that is used as a scalar observable for the system's dynamics. *Right:* Dimensionless values of the dynamic time step throughout the simulation. Cases shown in this figure use a constant discretization density with inter-nodal distance $h = 0.005$ corresponding to $N = 35\,222$ computational nodes.

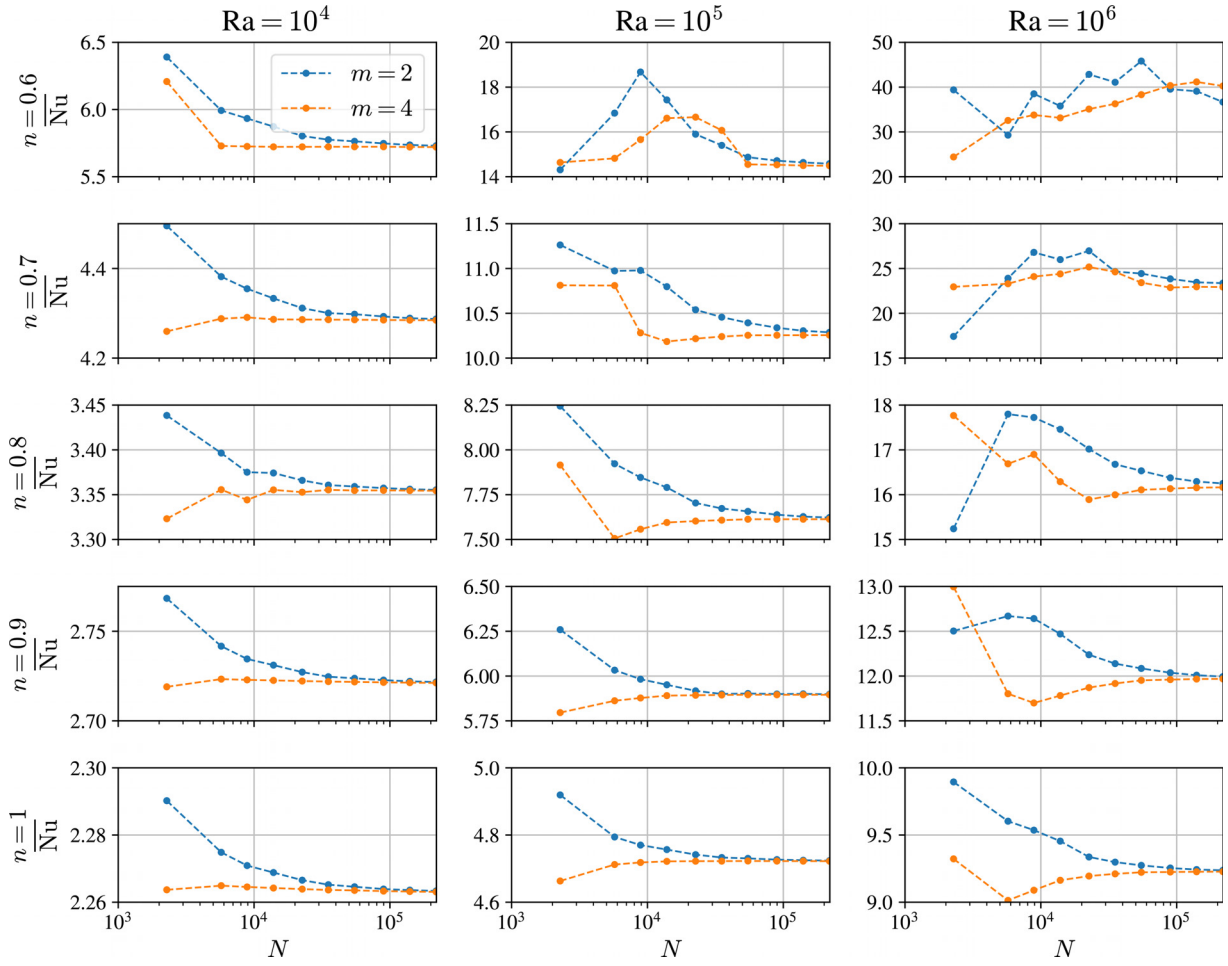

FIG. 6. Convergence of the average Nusselt number on the cold boundary with columns for all of the considered Ra and rows for different non-Newtonian exponents n. The two different considered monomial augmentation orders m are shown with different plot colors. Node count is proportional to the inter-nodal distance as the density is constant throughout the domain.

discretization in this intense region, while using much coarser discretization h_2 in the center of the domain, with a linear transition between the two

$$h = \begin{cases} h_1 & \text{where } d < w \\ h_1 + \dfrac{d-w}{L/2-w}(h_2 - h_1) & \text{otherwise.} \end{cases} \tag{25}$$

The value of the central inter-nodal distance

$$h_2 = \min(k_{\text{ref}} h_1, h_{\max}), \tag{26}$$

where k_{ref} is the refinement ratio that will be expressed as $\frac{h_2}{h_1}$ in subsequent analysis, is expressed in terms of minimal distance h_1 to prevent excessive density gradients that would require further analysis in terms of method stability and accuracy. Furthermore, h_2 is bounded with $h_{\max}$ to prevent instabilities. This relatively simple refinement scheme leads to drastic savings in node count shown in the right graph of Fig. 9. Even with the relatively conservative refinement parameters, there are almost an order of magnitude fewer nodes for the same boundary inter-nodal distances h_1. The slight non-linearity in the node count is caused by $h_{\max}$ limited h_2 when h_1 is large. The savings appear to be even more dramatic when a refined discretization is visually compared to an unrefined one as seen in Fig. 2.

We present an additional observation regarding the numerical method parameterization that can only be made when dealing with aggressively refined discretizations. The recommended support size $s > 2N_p$ for the approximation, corresponding to $s = 12$ in the analyzed case, is not sufficient to reach a stable solution for higher refinement ratios $\frac{h_2}{h_1}$ as shown in the left graph of Fig. 10. The results for the Ra $= 10^5$, Pr $= 100$, and $n = 0.6$ case calculated with $m = 2$ and $h_1 = 0.0025$ show that the range of stable refinement ratios raises with increasing support size until reaching $\frac{h_2}{h_1} = 25$ with $s = 15$. Based on this, we conservatively choose $s = 2.5N_p + 1$ rounded to the closest integer, corresponding to $s = 16$ in Fig. 10, as a rule for support size selection in the subsequent refined cases. The Nusselt number for the selected support size remained practically the same for the entire range of refinement ratios resulting in discretizations ranging from 140 134

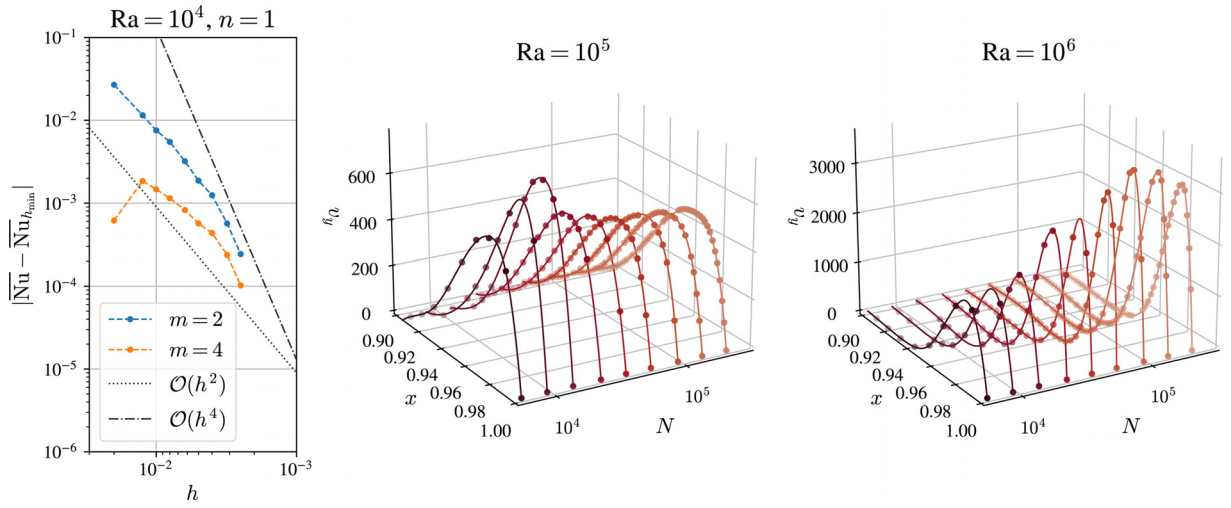

FIG. 7. *Left:* Convergence of average Nusselt number on the cold boundary toward the value calculated with the finest discretization that was used as the ground truth. *Middle and right:* Changes in the interpolated vertical velocity profiles close to the boundary at $y = 0.6$ with increasing number of uniformly positioned computational nodes. Cases shown are parametrized with $\mathrm{Pr} = 100$ and $n = 0.6$ and computed with $m = 2$. Dots display the horizontal position and vertical velocity in computational nodes that lie less than $\frac{h}{2}$ from the interpolation y.

nodes for $\frac{h_2}{h_1} = 1$ to 12 438 nodes for $\frac{h_2}{h_1} = 25$. Note that the $h_{\max}$ was not enforced for the discretization and that the dense band width was set to $w = 0$, further amplifying the impact of the changing node density on the boundary flow layer. The discrepancy between the different considered support sizes seen in Nusselt numbers on the left is also apparent from the vertical velocity cross sections shown on the right graph of Fig. 10 with the larger support sizes appearing to smoothen the velocity peak.

The refinement parameters, used in Fig. 9 and in other refined results with unspecified values, were chosen based on a convergence analysis. The analysis performed at $\mathrm{Ra} = 10^6$, $\mathrm{Pr} = 100$, and $n = 0.6$ would need to be repeated for other cases with significant differences in boundary layer thickness and other flow characteristics. Refinement parameters have been individually varied for different border densities with the results shown in Fig. 11.

We assume that a further refinement in parameters would not lead to significant changes, and therefore we norm the Nusselt number, shown in the upper graphs, to the best present value. Normalized values allow for comparison between cases with a different maximum density and conveniently show the relative offset in value.

The refinement ratio $\frac{h_2}{h_1}$ sweep is performed with a band width $w = 0.05$ that is wide enough to not have a meaningful impact on the results as established in the following paragraph. The resulting Nusselt numbers, shown in the upper left graph of Fig. 11, are relatively unaffected by the refinement ratio, as long as the resulting h_2 is small enough to ensure numerical stability. Results are stable, with variations within 1%. We chose $\frac{h_2}{h_1} = 20$ as a conservative choice for refinement aggressiveness, corroborated with Fig. 10 for the selected support size. The conservative choice of refinement ratio is justified by the graph of computational node count dependence, shown in the lower left graph of Fig. 11, where we can see that further increasing refinement ratio leads to diminishing reduction in the number of computational nodes. This analysis is also used to set the $h_{\max} = 0.05$ based on refinement ratios where stable solution was no longer achieved.

The dense boundary width w sweep is calculated with a refinement ratio of $\frac{h_2}{h_1} = 10$, that has been determined to be adequate in the previous paragraph, and the results are shown in the upper right graph of Fig. 11. The main goal of the dense boundary band is providing a sufficient discretization for the high velocity flow and the corresponding gradients in the boundary layer. We can use Fig. 7 to estimate the required width to 0.02–0.03, based on the distance from the boundary where flow velocity reduces to half its maximum value. The estimate is confirmed with numerical results that show no improvement when increasing the boundary band width w beyond a point where it covers the boundary layer flow. The effect of w is less noticeable when using smaller h_1 as the linearly decreasing density beyond the edge of the dense band still provides a sufficient density as long as the peak of the flow is covered. We chose $w = 0.025$ as the refinement parameter for further use as it provides practically the same results as $w = 0.1$, especially at smaller h_1 that we are mainly interested in, while providing a significant reduction in node count as seen from the lower right graph of Fig. 11.

The symmetric refinement approach is not ideal, but is suitable as a proof-of-concept due to the small number of density function parameters, which simplifies their analysis and selection. A simple improvement would be to treat the non-insulated and insulated boundaries differently, since the latter do not exhibit the sharp convective flow layer and can be discretized with a lower density. The real improvements to refinement can become arbitrary complex and focus on deriving an error indicator based either on a previous, less refined solution or on the properties of the numerical method itself.

We use the refined density to recalculate the convergence for $\mathrm{Ra} = 10^6$ and $n = 0.6$ case that did not converge with the constant density discretization. The new convergence results are shown in Fig. 12 for the two different considered augmentation orders m. Not only is convergence achieved, but it is also achieved with a significantly smaller number of nodes and with a drastically reduced symmetry error. The computational times are shown in Table I to further emphasize that the reduction in the number of computational nodes

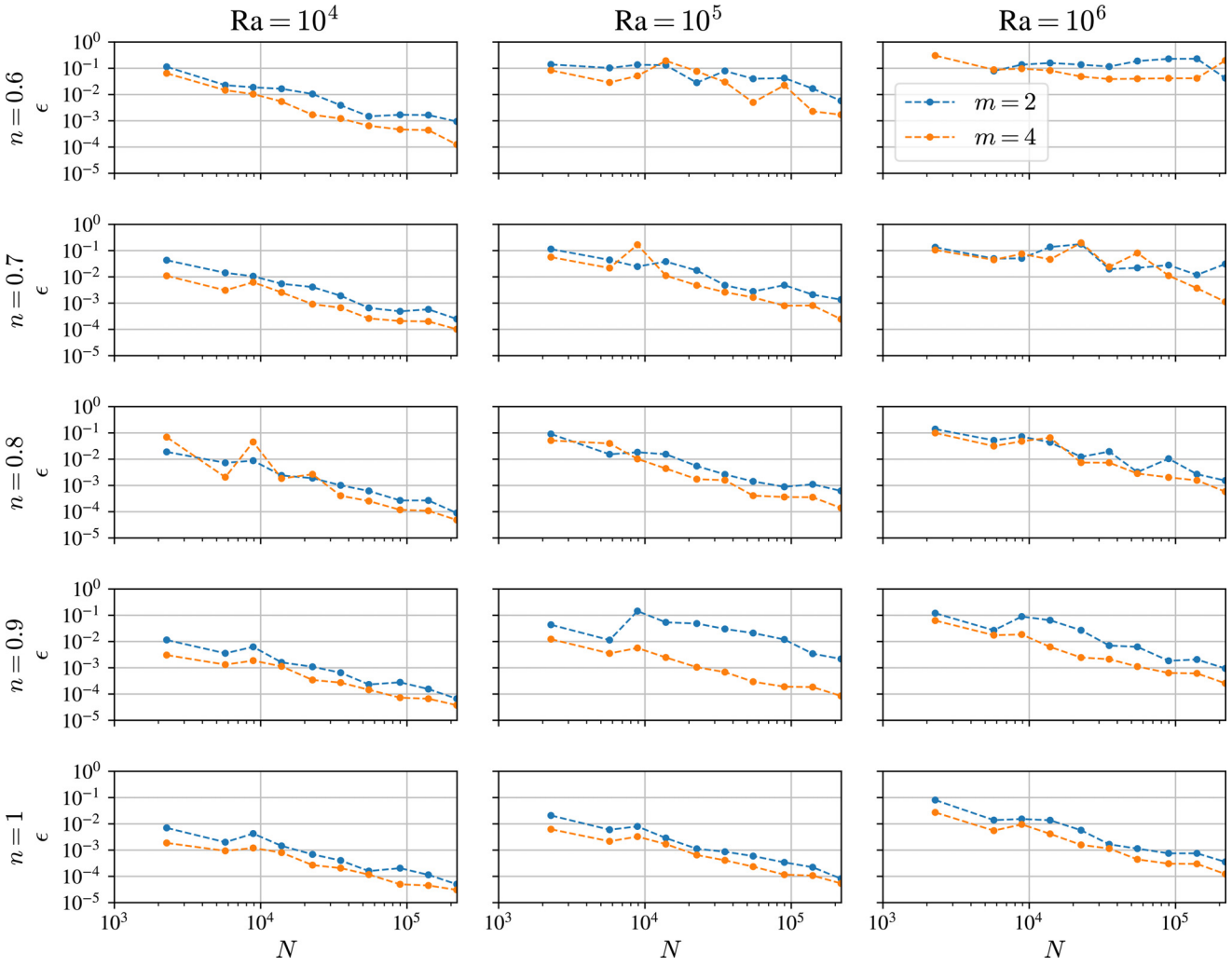

FIG. 8. Convergence of the relative symmetry error at $y = 0.75$ with columns for all of the considered Ra and rows for different non-Newtonian exponents *n*. The two different considered monomial augmentation orders *m* are shown with different plot colors. Node count is proportional to the inter-nodal distance as the density is constant throughout the domain.

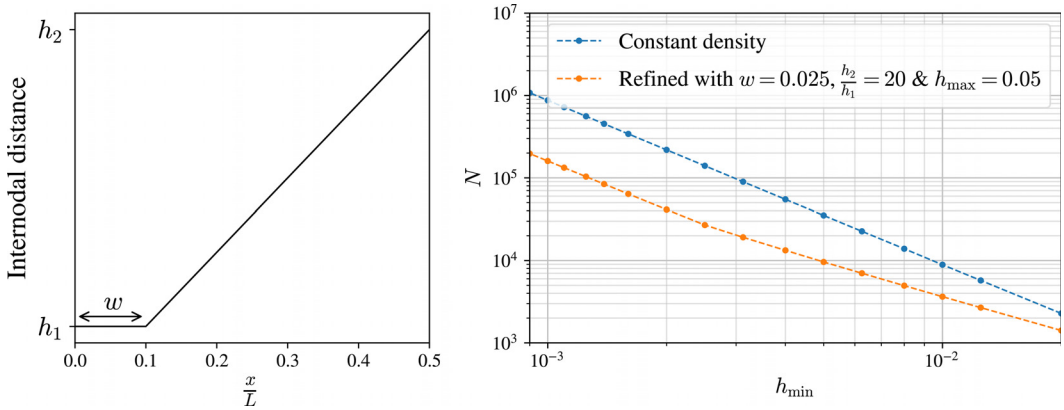

FIG. 9. *Left:* A schematic representation of the inter-nodal distance as a function of distance from the boundary. *Right:* Computational node count as a function of minimum inter-nodal distance for a constant density and a refined case.

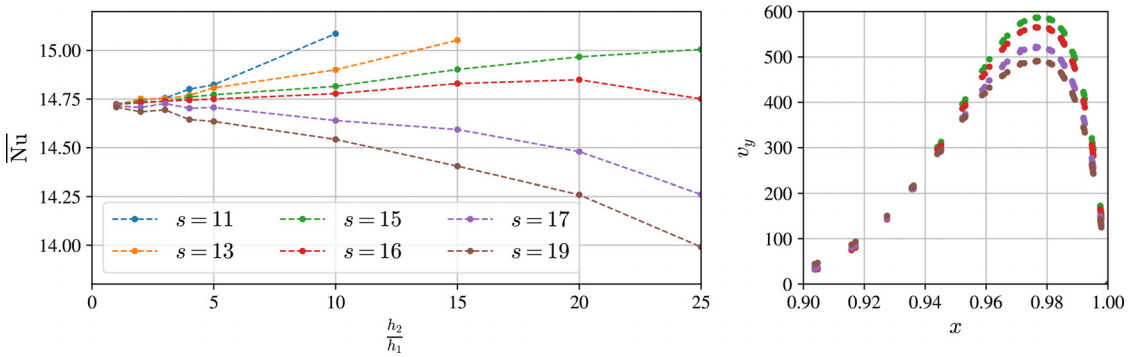

FIG. 10. *Left:* The average Nusselt number on the cold wall as a function of refinement ratio $\frac{h_2}{h_1}$ for different support sizes s. *Right:* Vertical velocity cross section close to the right wall at $y = 0.5$ corresponding to the rightmost cases from the left graph with $\frac{h_2}{h_1} = 25$ and different support sizes s. The cross section shows values in nodes closer than $5h_1$ in y coordinate. Support sizes are chosen as $s = k_s N_p + 1$, rounded to the closest integer for $k_s \in \{1.75, 2, 2.25, 2.5, 2.75, 3\}$.

translates into savings in computational time required. Even with the increased support size, the refined discretization still provides a solution in more than ten times shorter time than the unrefined. The timing was performed on four cores of `Intel(R) Xeon(R) E5520` CPU with the frequency fixed to 2.27 GHz.

D. Comparison with reference data

Non-Newtonian fluid dynamics in a differentially heated cavity have already been tackled previously, and we have performed our study on a matching case for verification. We use the results provided by Turan *et al.*[13] and Kim *et al.*,[12] who used FVM with SIMPLE coupling and Upwind or QUICK stabilization. We compare those results with a refined RBF-FD and ACM, without stabilization of convective terms to minimize the effect of numerical diffusion.

Both publications provide an empirical fit for the average Nusselt number as a function of Rayleigh number Ra, Prandtl number Pr, and non-Newtonian exponent n,

$$\overline{\mathrm{Nu}}_{\mathrm{Turan}} = 0.162\mathrm{Ra}^{0.043}\frac{\mathrm{Pr}^{0.341}}{(1+\mathrm{Pr})^{0.091}}\left(\frac{\mathrm{Ra}^{(2-n)}}{\mathrm{Pr}^{n}}\right)^{\frac{1}{2(n+1)}}\exp(\mathrm{C}(n-1)), \tag{27}$$

$$\mathrm{C} = \begin{cases} 1.343\mathrm{Ra}^{0.065}\mathrm{Pr}^{0.036} & \text{where } n \leq 1 \\ 0.858\mathrm{Ra}^{0.071}\mathrm{Pr}^{0.034} & \text{otherwise,} \end{cases} \tag{28}$$

$$\overline{\mathrm{Nu}}_{\mathrm{Kim}} = 0.3n^{0.4}\mathrm{Ra}^{\frac{1}{3n+1}}, \tag{29}$$

that we can use to compare against our results.

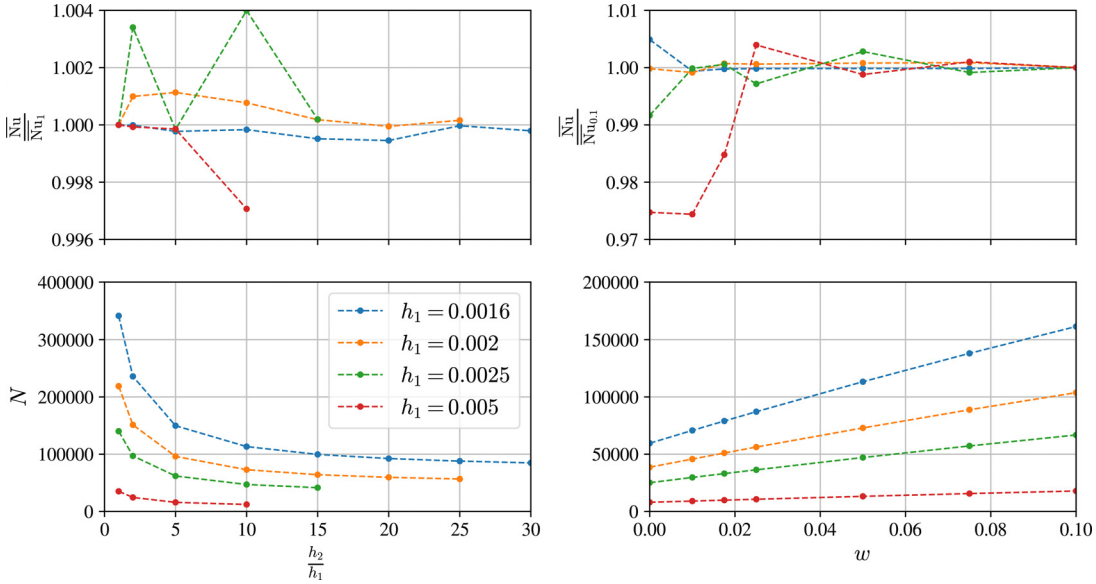

FIG. 11. Impact of refinement scheme parameter variation on the Nusselt number shown in the top and node count in the bottom graphs. Nusselt values are normed to the value attained with the best considered parameter value. *Left:* Variation of the refinement ratio $\frac{h_2}{h_1}$ with the dense boundary band held constant at $w = 0.05$. *Right:* Variation of the dense boundary band w with the refinement ratio held constant at $\frac{h_2}{h_1} = 10$.

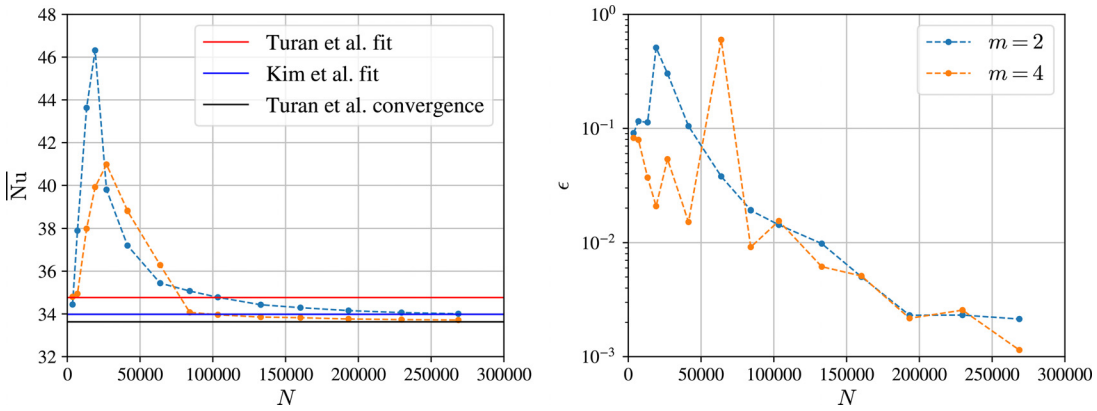

FIG. 12. *Left:* Convergence study for the problematic Ra $= 10^6$, Pr $= 100$, and $n = 0.6$ case repeated with a refined density. Red and blue horizontal lines show Nusselt values derived from correlations defined in Eqs. (28) and (29), while the black shows the best value from the convergence study presented in Turan *et al.*[13] *Right:* The relative symmetry error for the repeated convergence study.

TABLE I. A table comparing computational time (bold) and other properties for the refined and the unrefined discretization with different approximation orders in the Ra $= 10^6$, Pr $= 100$, and $n = 0.6$ case.

	h_1	h_2	N	m	s	$\overline{\mathrm{Nu}}$	t (h)
Refined	0.0025	0.05	26961	2	16	39.8	**5**
				4	39	41.0	**9**
Unrefined		0.0025	140134	2	13	38.8	**63**
				4	31	41.0	**182**

The Nusselt values calculated by the provided correlations are added to Fig. 12, supplemented by the exact numerical value from the convergence study performed by Turan *et al.* on this case. All results agree well, with small deviations that are normal due to discretization errors and different numerical methods. We must also keep in mind that the provided correlations, in all their complexity, are still only empirical fits over a wide range of flow regimes and are a rather crude approximation, as can be seen from the relatively large discrepancy between the Turan *et al.* fit and the convergence value from the corresponding study.

We extend the fit comparison to all cases considered with the results shown in Fig. 13. All computed values fall within the range of the provided correlation functions, again confirming that the meshless RBF-FD method yields valid results. The relative difference between the fits increases significantly for calmer cases with a smaller Nusselt number, casting further doubt on the accuracy of the empirical fits for a wide range of parameters. The case-dependent discrepancy between our numerical results and the provided fits is similar to that in the source publication.

We also tested different monomial orders for the entire range of considered cases shown in Fig. 13. The difference between the results computed with augmentation orders is in all cases smaller than the difference between Turan *et al.* and Kim *et al.*, which means that the lower order $m = 2$ is adequate for a stable and accurate computation when the discretization is sufficiently dense. Whether using higher

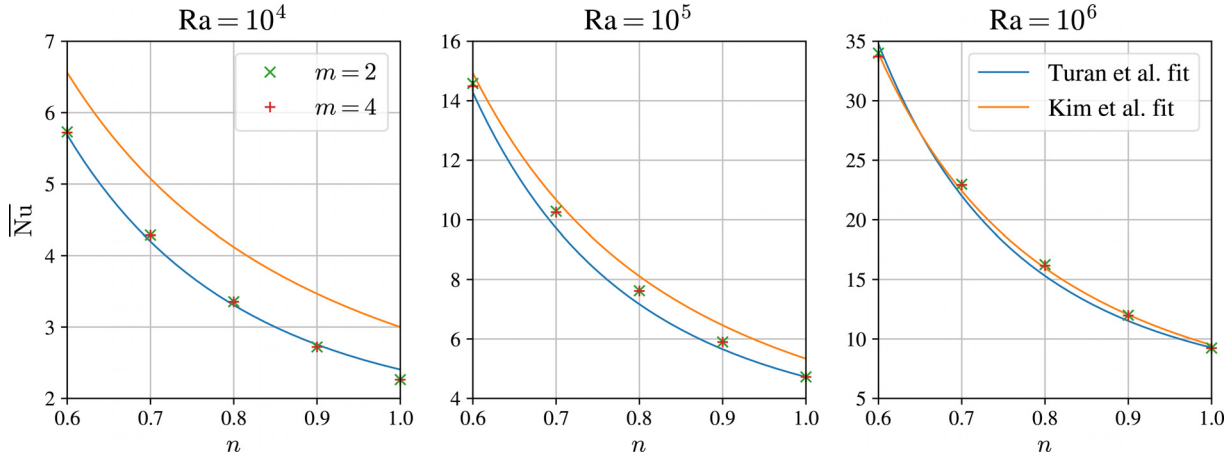

FIG. 13. Comparison between the calculated Nusselt values and correlations provided in existing literature. Solid lines represent correlations defined in Eqs. (28) and (29).

TABLE II. A table of the best obtained average Nusselt values for all of the considered parameters. Presented values are calculated with $m = 2$. Refined density discretization is used for the problematic $\mathrm{Ra} = 10^6$ and $n \in \{0.6, 0.7\}$ cases.

Ra	$n = 0.6$	$n = 0.7$	$n = 0.8$	$n = 0.9$	$n = 1$
10^4	5.72	4.28	3.35	2.72	2.26
10^5	14.49	10.26	7.61	5.90	4.72
10^6	33.71	22.92	16.16	11.97	9.23

order method is beneficial is case dependent as can be seen from Fig. 6. Cases with lower Ra, where resolution of the boundary layer is not problematic, appear to benefit from the higher order by reaching node density independent result at a drastically lower node count. The opposite is true for the high Ra and low n cases where increasing the order is at times counterproductive. Using a higher order method appears beneficial for the refined discretization cases shown in Fig. 12, but the final benefits of increasing the augmentation order are again case dependent and require additional analysis to determine optimal compromise between the lower total number of computational nodes and the increased computational time required per computational node.

We report the average Nusselt value at the cold boundary calculated with the finest discretization for the full range of considered parameters at $\mathrm{Pr} = 100$ in Table II.

V. GEOMETRICAL FLEXIBILITY

Finally, we apply the described solution procedure to more complex domains in order to demonstrate the geometrical flexibility that we touted as one of the main benefits. In the first example, shown in Fig. 14, we add circular obstructions to the central part of the De Vahl Davis case to simulate how the non-Newtonian behavior would impact the convective flow passing through a porous filter. The computational node distribution used in this case, shown in the right panel of Fig. 2, utilizes a modified refinement strategy that increases node density in narrow channels and on nearby boundaries to ensure that at least two computational nodes discretize the channel's width. Even though the dimensionless numbers defined in Sec. II are no longer suitable for this case, we stick with them to enable comparison with unobstructed flow profiles shown in Fig. 3. We use the same random filter configuration for the shear-thinning non-Newtonian fluid on the left and the Newtonian fluid on the right graph of Fig. 14. The results are unsurprising with both the change in temperature profile and the reduction of maximum velocity confirming that the filter's narrow channels present a far greater hindrance for the Newtonian fluid. This can further be confirmed by comparing the average Nusselt number on the cold wall against the unobstructed case with the same $h = 0.008$ discretization. The $\overline{\mathrm{Nu}}$ value decreases in both cases, indicating weaker convective heat transfer, but the change in the non-Newtonian $n = 0.6$ case from 35.8 to 35 is almost negligible, while the $\overline{\mathrm{Nu}}$ value practically halves from 9.5 to 4.8 in the Newtonian $n = 1$ case.

The shear-thinning filter case presents a suitable opportunity to examine the spatial variation in viscosity shown in Fig. 15. We show the inverse of viscosity to better highlight the shear-thinning aspect with the most affected areas corresponding to edges of the high velocity layer next to the vertical walls and in high velocity channels through the filter as seen in Fig. 14. Viscosity behavior next to the vertical walls is identical to the non-filter cases.

We formulated the method in a dimensionally agnostic manner, which can be with some effort directly transformed into dimensionally

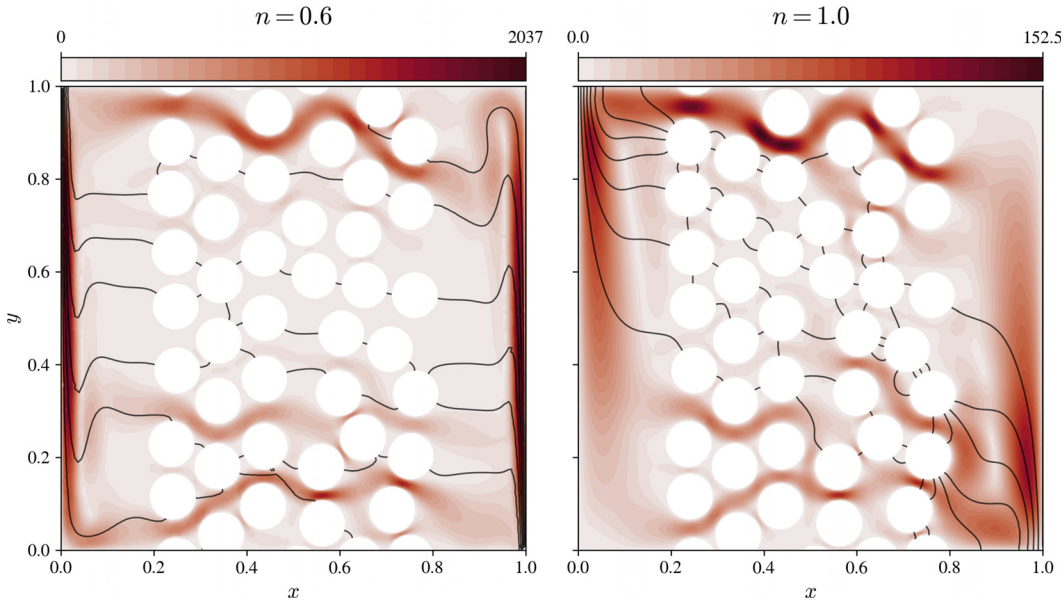

FIG. 14. Flow profiles for $\mathrm{Ra} = 10^6$ and $\mathrm{Pr} = 100$ case with a porous central section. Velocity magnitude is visualized with a heat-map, while the overlaid contours display the changes in temperature. The strongest shear-thinning $n = 0.6$ case is shown on the left sub-figure, while the right displays the Newtonian $n = 1$ case.

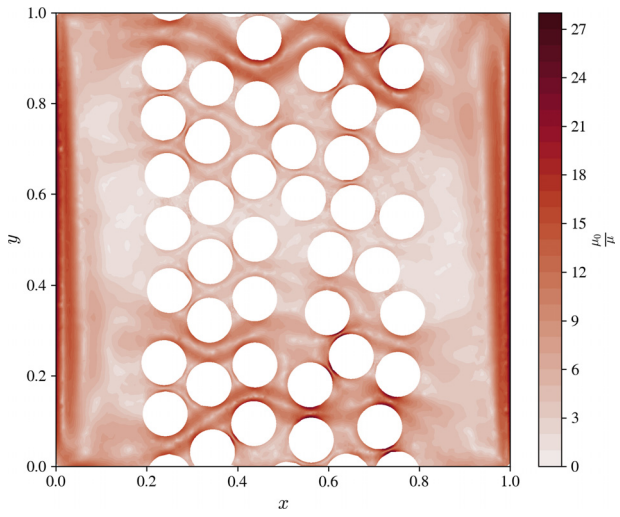

FIG. 15. Variation in viscosity due to shear-thinning effects. Higher values signify lower viscosity due to the normed inverse visualization that is chosen to highlight the areas where shear rate caused thinning is the strongest.

agnostic object-oriented code design,[50] using powerful C++ template systems. The filtered 2D case can thus be quickly transformed into its 3D variant shown in Fig. 16 with minimal interference in the core code that is limited only to the parameters (refer to the supplied repository[51] for the actual code). For better visual representation plane intersections of the vertical velocity, temperature and viscosity are presented in Fig. 17. The purpose of presenting these 3D results is twofold. First, we want to demonstrate the ability of the presented method to address a complex physical problem on an irregular 3D domain. Second, we want to demonstrate the powerful concept of merging the generally formulated RBF-FD method with a generic programing to design a dimension independent solution procedure. More details on the C++ implementation aspect can be found in Ref. 50.

VI. CONCLUSIONS

In this paper, we have proposed a dimension independent refined meshless solution procedure for NNC. The main advantage of the proposed approach is that it can operate on scattered nodes, which greatly facilitates the consideration of complex 3D domains and the implementation of refined discretization, both of which are demonstrated in this paper. Moreover, the approximation weights are computed individually, allowing for a variation in the stencil size s, monomial augmentation order m, the type and order of the RBFs used, etc. The ease of adaptation on all mentioned levels allows the use of a sophisticated but slow approximation only where it is truly needed with faster alternatives elsewhere, which is often the majority of the domain when dealing with realistic cases.

From the meshless method point of view, we have shown that the method is appropriate for the considered problem given that the discretization is sufficiently dense to describe the present flow structures. We have shown how the problems with inadequate discretization manifest themselves and how they can be resolved by refinement. We have shown that the proposed solution procedure allows for an aggressively refined discretization that can be pushed even further if the support size is slightly increased from the usual recommendation, leading to an order of magnitude lower computational times.

From the non-Newtonian fluid dynamics point of view, we presented new results for the benchmark case that is already solved with two similar FVM approaches[12,13] with a fundamentally different numerical approach and, most importantly, without stabilization, that effectively introduces numerical diffusion in the solution.

In future work, we will expand the analysis of how the interplay between node density and stencil size influences sharp flow structures, like the boundary layer shown in this paper, and attempt to determine what are the requirements for an accurate reproduction. We will use this knowledge to develop an h-adaptive solution, which requires an adequate error indicator and a refinement logic that constructs the target node density function from the error indicator data and refines the nodes accordingly.[27]

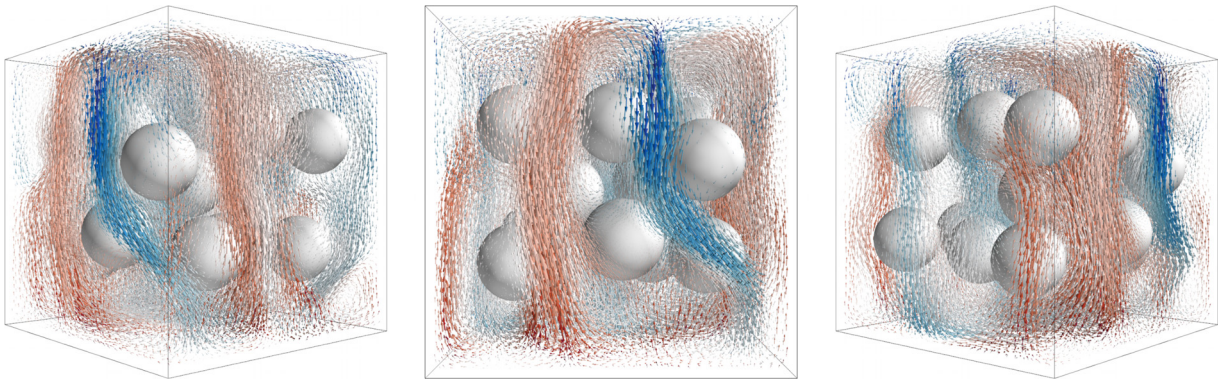

FIG. 16. Natural convection in a 3D differentially heated cavity with obstructions. This case differs from the previous as the temperature differential and resulting flow is now vertical. The glyphs are sized according to the velocity magnitude in the computational node and colored according to the temperature complying with the colorbar in Fig. 17.

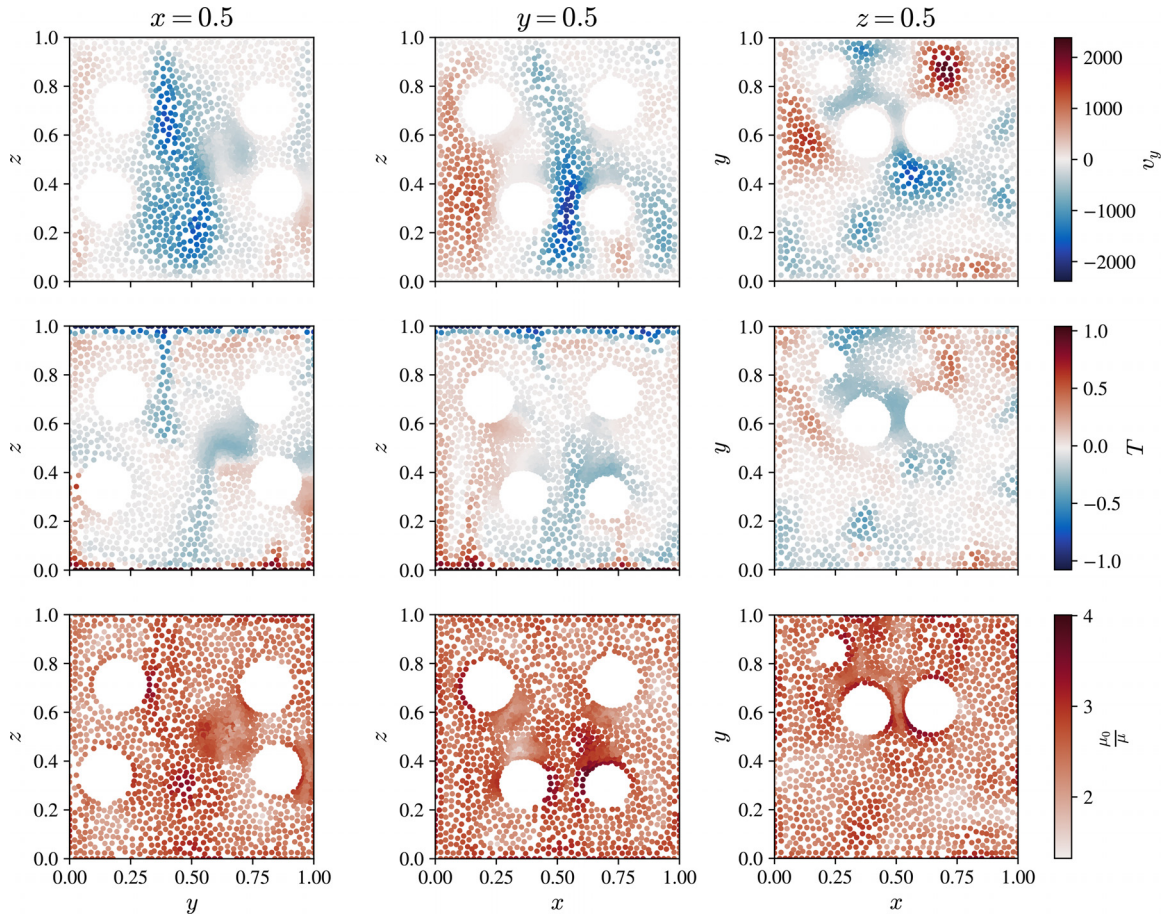

FIG. 17. Plane intersections of the 3D case shown in Fig. 16. The first row displays vertical velocity, the second row displays the temperature, and the third row displays the inverse of the shear-thinning viscosity. Values and positions shown on the scatterplot correspond to computational nodes within $\frac{h}{2}$ of the intersecting plane.

In addition, we also plan to analyze how hyperviscosity[52] and adaptive upwind[53] stabilizations, and using different approximation approaches[54] affect the flow structures.

ACKNOWLEDGMENTS

The authors would like to acknowledge the financial support of the Slovenian Research and Innovation Agency (ARIS) research core Funding No. P2-0095, Young Researcher programme PR-10468, and project funding N2-0275. Funded by the National Science Centre, Poland under the OPUS call in the Weave programme 2021/43/I/ST3/00228. This research was funded in whole or in part by the National Science Centre (2021/43/I/ST3/00228). For the purpose of Open Access, the author has applied a CC-BY public copyright licence to any Author Accepted Manuscript (AAM) version arising from this submission.

AUTHOR DECLARATIONS

Conflict of Interest

The authors have no conflicts to disclose.

Author Contributions

Miha Rot: Conceptualization (supporting); Data curation (lead); Formal analysis (lead); Investigation (lead); Methodology (equal); Software (lead); Validation (lead); Visualization (lead); Writing – original draft (lead); Writing – review & editing (supporting). **Gregor Kosec:** Conceptualization (lead); Funding acquisition (lead); Methodology (equal); Resources (lead); Supervision (lead); Validation (supporting); Writing – original draft (supporting); Writing – review & editing (lead).

DATA AVAILABILITY

The data that support the findings of this study are openly available in Zenodo and GitLab repository at http://doi.org/10.5281/zenodo.14901942, Refs. 55 and 51.

REFERENCES

[1]A. Rahimi, A. Dehghan Saee, A. Kasaeipoor, and E. Hasani Malekshah, "A comprehensive review on natural convection flow and heat transfer," Int. J. Numer. Methods Heat Fluid Flow **29**(3), 834–877 (2019).

[2]A. Bejan, *Convection Heat Transfer* (John Wiley & Sons, 2013).
[3]R. P. Chhabra, *Non-Newtonian Fluids: An Introduction* (Springer New York, New York, NY, 2010), pp. 3–34.
[4]X. Wang and X. Li, "Numerical simulation of three dimensional non-Newtonian free surface flows in injection molding using ALE finite element method," Finite Elem. Anal. Des **46**(7), 551–562 (2010).
[5]S. Charm and G. Kurland, "Viscometry of human blood for shear rates of 0-100,000 sec-1," Nature **206**, 617–618 (1965).
[6]A. C. A. Gratão, V. Silveira, and J. Telis-Romero, "Laminar flow of soursop juice through concentric annuli: Friction factors and rheology," J. Food Eng. **78**(4), 1343–1354 (2007).
[7]J. Welti-Chanes, F. Vergara-Balderas, and D. Bermúdez-Aguirre, "Transport phenomena in food engineering: Basic concepts and advances," J. Food Eng. **67**(1–2), 113–128 (2005).
[8]E. C. Bingham, *An Investigation of the Laws of Plastic Flow* (US Government Printing Office, 1917).
[9]L. Yang and K. Du, "A comprehensive review on the natural, forced, and mixed convection of non-Newtonian fluids (nanofluids) inside different cavities," J. Therm. Anal. Calorim. **140**, 2033–2054 (2020).
[10]J. Kwack and A. Masud, "A stabilized mixed finite element method for shear-rate dependent non-Newtonian fluids: 3D benchmark problems and application to blood flow in bifurcating arteries," Comput. Mech. **53**, 751–776 (2014).
[11]S. Patankar, *Numerical Heat Transfer and Fluid Flow* (Taylor & Francis, London, 1980).
[12]G. B. Kim, J. M. Hyun, and H. S. Kwak, "Transient buoyant convection of a power-law non-Newtonian fluid in an enclosure," Int. J. Heat Mass Transfer **46**(19), 3605-3617 (2003).
[13]O. Turan, A. Sachdeva, N. Chakraborty, and R. J. Poole, "Laminar natural convection of power-law fluids in a square enclosure with differentially heated side walls subjected to constant temperatures," J. Non-Newtonian Fluid Mech. **166**(17–18), 1049–1063 (2011).
[14]M. V. Bozorg and M. Siavashi, "Two-phase mixed convection heat transfer and entropy generation analysis of a non-Newtonian nanofluid inside a cavity with internal rotating heater and cooler," Int. J. Mech. Sci. **151**, 842–857 (2019).
[15]N. O. Moraga, M. A. Marambio, and R. C. Cabrales, "Geometric multigrid technique for solving heat convection-diffusion and phase change problems," Int. Commun. Heat Mass Transfer **88**, 108–119 (2017).
[16]D. A. Vasco, N. O. Moraga, and G. Haase, "Parallel finite volume method simulation of three-dimensional fluid flow and convective heat transfer for viscoplastic non-Newtonian fluids," Numer. Heat Transfer, Part A **66**(9), 990–1019 (2014).
[17]D. S. Loenko, A. Shenoy, and M. A. Sheremet, "Natural convection of non-Newtonian power-law fluid in a square cavity with a heat-generating element," Energies **12**(11), 2149 (2019).
[18]A. Alsabery, A. Chamkha, H. Saleh, and I. Hashim, "Transient natural convective heat transfer in a trapezoidal cavity filled with non-Newtonian nanofluid with sinusoidal boundary conditions on both sidewalls," Powder Technol. **308**, 214 (2017).
[19]L. Mishra and R. P. Chhabra, "Natural convection in power-law fluids in a square enclosure from two differentially heated horizontal cylinders," Heat Transfer Eng. **39**, 819 (2018).
[20]G. R. Kefayati, "Simulation of magnetic field effect on natural convection of non-Newtonian power-law fluids in a sinusoidal heated cavity using FDLBM," Int. Commun. Heat Mass Transfer **53**, 139 (2014).
[21]G.-R. Liu, *Mesh Free Methods: Moving Beyond the Finite Element Method* (CRC Press, 2002).
[22]A. I. Tolstykh and D. A. Shirobokov, "On using radial basis functions in a 'finite difference mode' with applications to elasticity problems," Comput. Mech. **33**, 68 (2003).
[23]J. Slak and G. Kosec, "On generation of node distributions for meshless PDE discretizations," SIAM J. Sci. Comput. **41**, A3202 (2019).
[24]W. Trojak, N. Vadlamani, J. Tyacke, F. Witherden, and A. Jameson, "Artificial compressibility approaches in flux reconstruction for incompressible viscous flow simulations," Comput. Fluids **247**, 105634 (2022).
[25]G. Kosec, "A local numerical solution of a fluid-flow problem on an irregular domain," Adv. Eng. Software **120**, 36 (2018).
[26]T. Yasuda, I. Tanno, T. Hashimoto, K. Morinishi, and N. Satofuka, "Artificial compressibility method using bulk viscosity term for an unsteady incompressible flow simulation," Comput. Fluids **258**, 105885 (2023).
[27]J. Slak and G. Kosec, "Adaptive radial basis function-generated finite differences method for contact problems," Int. J. Numer. Methods Eng. **119**, 661 (2019).
[28]M. Jančič, J. Slak, and G. Kosec, "p-refined RBF-FD solution of a Poisson problem," in *6th International Conference on Smart and Sustainable Technologies (SpliTech)* (IEEE, 2021), pp. 01–06.
[29]J. D. Anderson, Jr., *Fundamentals of Aerodynamics* (Tata McGraw-Hill Education, 2010).
[30]D. J. Tritton, *Physical Fluid Dynamics* (Oxford Science Publication, Clarendon Press, 1988).
[31]The shear rate tensor for incompressible fluids is the same as the strain rate tensor, which can be expressed as the symmetric part of the velocity gradient.
[32]The limit is arbitrarily chosen and has a negligible effect on the result.[12]
[33]G. De Vahl Davis, "Natural convection of air in a square cavity: A bench mark numerical solution," Int. J. Numer. Methods Fluids **3**, 249 (1983).
[34]D. P. Hardin and E. B. Saff, "Discretizing manifolds via minimum energy points," Not. AMS **51**, 1186 (2004).
[35]V. Shankar, R. M. Kirby, and A. L. Fogelson, "Robust node generation for mesh-free discretizations on irregular domains and surfaces," SIAM J. Sci. Comput. **40**(4), 2584–2608 (2018).
[36]M. Depolli, J. Slak, and G. Kosec, "Parallel domain discretization algorithm for RBF-FD and other meshless numerical methods for solving PDEs," Comput. Struct. **264**, 106773 (2022).
[37]U. Duh, G. Kosec, and J. Slak, "Fast variable density node generation on parametric surfaces with application to mesh-free methods," SIAM J. Sci. Comput. **43**, A980 (2021).
[38]U. Duh, V. Shankar, and G. Kosec, "Discretization of non-uniform rational B-spline (NURBS) models for meshless isogeometric analysis," J. Sci. Comput. **100**, 51 (2024).
[39]O. Davydov, D. T. Oanh, and N. M. Tuong, "Improved stencil selection for meshless finite difference methods in 3D," J. Comput. Appl. Math. **425**, 115031 (2023).
[40]N. Flyer, B. Fornberg, V. Bayona, and G. A. Barnett, "On the role of polynomials in RBF-FD approximations: I. Interpolation and accuracy," J. Comput. Phys. **321**, 21 (2016).
[41]The 6 monomials in 2-D case with $m = 2$ would be $q = \{1, x, y, x^2, xy, y^2\}$.
[42]M. Jančič, J. Slak, and G. Kosec, "Monomial augmentation guidelines for RBF-FD from accuracy versus computational time perspective," J. Sci. Comput. **87**, 9 (2021).
[43]S. L. Borne and W. Leinen, "Guidelines for RBF-FD discretization: Numerical experiments on the interplay of a multitude of parameter choices," J. Sci. Comput. **95**, 8 (2023).
[44]V. Bayona, N. Flyer, B. Fornberg, and G. A. Barnett, "On the role of polynomials in RBF-FD approximations: II. Numerical solution of elliptic PDEs," J. Comput. Phys. **332**, 257 (2017).
[45]M. Jančič and G. Kosec, "Strong form mesh-free hp-adaptive solution of linear elasticity problem," Eng. Comput. **40**, 1027 (2023).
[46]A. J. Chorin, "A numerical method for solving incompressible viscous flow problems," J. Comput. Phys. **2**, 12 (1967).
[47]G. Kosec, M. Depolli, A. Rashkovska, and R. Trobec, "Super linear speedup in a local parallel meshless solution of thermo-fluid problems," Comput. Struct. **133**, 30 (2014).
[48]A. Kajzer and J. Pozorski, "Application of the entropically damped artificial compressibility model to direct numerical simulation of turbulent channel flow," Comput. Math. Appl. **76**, 997 (2018).
[49]M. M. Rahman and T. Siikonen, "An artificial compressibility method for viscous incompressible and low Mach number flows," Int. J. Numer. Methods Eng. **75**, 1320 (2008).
[50]J. Slak and G. Kosec, "Medusa: A C++ library for solving PDES using strong form mesh-free methods," ACM Trans. Math. Software **47**, 1 (2021).
[51]Gitlab Repository, see https://gitlab.com/e62Lab/public/2022_p_refinednon-newtonianconvection for "Refined Radial Basis Function-Generated Finite Difference Analysis of Non-Newtonian Natural."

[52]V. Shankar and A. L. Fogelson, "Hyperviscosity-based stabilization for radial basis function-finite difference (RBF-FD) discretizations of advection–diffusion equations," J. Comput. Phys. **372**, 616 (2018).
[53]G. Kosec and B. Šarler, "Simulation of macrosegregation with mesosegregates in binary metallic casts by a meshless method," Eng. Anal. Boundary Elem. **45**, 36 (2014).
[54]V. Hatič, B. Mavrič, and B. Šarler, "Meshless simulation of a lid-driven cavity problem with a non-Newtonian fluid," Eng. Anal. Boundary Elem. **131**, 86 (2021).
[55]M. Rot and G. Kosec (2025). "Refined radial basis function-generated finite difference analysis non-Newtonian natural convection," Zenodo, Dataset, https://doi.org/10.5281/zenodo.14901943